Chapter 8

Mechanochemical Synthesis of Water-Based Magnetite Magnetic Fluids

Tomohiro Iwasaki

Additional information is available at the end of the chapter

http://dx.doi.org/10.5772/66075

Abstract

Magnetite, Fe_3O_4 ($Fe^{II}O$-$Fe^{III}_2O_3$), is a member of the spinel group as well as a common ferrite with a cubic inverse spinel structure. Aqueous colloidal solutions of Fe_3O_4, i.e. water-based Fe_3O_4 magnetic fluids, have attracted substantial attention in biomedical applications, such as drug delivery, magnetic resonance imaging, and magnetic hyperthermia. In this study, to readily prepare water-based magnetic fluids with biocompatible dispersant-coated Fe_3O_4 nanoparticles that are stably dispersed in water medium, a mechanochemical synthesis method was developed. In this method, an iron-free citric acid solution is milled in a tumbling ball mill with steel balls at room temperature, reducing the production costs and environmental impacts. The initial gas phase in the milling vessel is air, and pressure is varied to control the formation of Fe_3O_4 nanoparticles. Although no iron species are contained in the starting solution, Fe_3O_4 nanoparticles form in the solution according to the reaction mechanism based on the oxidation-reduction processes of the corrosion of steel. At the same time, the Fe_3O_4 nanoparticle surface is modified with citrate ions, resulting in a stable dispersion. The magnetic fluids prepared using this mechanochemical method possess good induction heating properties in an alternating current magnetic field.

Keywords: magnetite nanoparticles, inverse spinel, magnetic fluid, mechanochemical reaction, oxidation-reduction, hyperthermia

1. Introduction

Magnetic fluids are colloidal solutions containing magnetic nanoparticles stably dispersed in a liquid medium so that the entire fluid behaves like a ferromagnet. Moreover, no solid-liquid

separation occurs, even under centrifugal force fields [1]. Therefore, magnetic fluids are widely used in industrial products, such as rotating-axis seal material, lubricants, and liquid damper. In magnetic fluids, iron-based oxide nanoparticles are often employed as the magnetic material. In particular, magnetic fluids that consist of superparamagnetic magnetite (Fe_3O_4) nanoparticles are used in biomedical and environmental fields, such as magnetic resonance imaging (MRI) contrast agents [2], magnetic hyperthermia in cancer therapy [3], drug delivery systems (DDS) [4], and so on, due to their high performance, low toxicity, and low environmental impact. The appropriate size of the Fe_3O_4 nanoparticles depends on their application. For example, when used for MRI, hyperthermia, and DDS, the particle size is required to be below 30 nm. Appropriate surface modification of the Fe_3O_4 nanoparticles can bind them to biomolecules as a result of the large surface area, leading to good bio-circulation [5]. In addition, the enhanced permeability and retention (EPR) effect can selectively accumulate Fe_3O_4 nanoparticles into cancer tissue [6]. Accordingly, the sizes of primary particles and aggregates must be controlled, and good stable dispersion is needed. Therefore, many studies on controlling the particle size as well as dispersion and aggregation using additives and organic solvents have been conducted. Wen et al. [7] prepared Fe_3O_4 nanoparticles with a size of 4–5 nm in an organic solvent by adding sodium oleate as a surfactant. Zhang et al. [8] synthesized Fe_3O_4 nanoparticles with good dispersibility in an organic solvent using surface modification with polystyrene. Frimpong et al. [9] controlled the sizes of the primary particle and aggregate using citric acid. Elisa de Sousa et al. [10] obtained citrate-adsorbed Fe_3O_4 nanoparticles that were dispersed under neutral conditions. In Fe_3O_4 nanoparticles that are used in vivo, biocompatible molecules, such as dextran, polyethylene glycol, polyvinyl alcohol, citric acid, polyacrylic acid, and phospholipid, are frequently employed as additives. In particular, citric acid is non-toxic and can form ultrafine primary particles. Furthermore, citrate ions can adsorb onto Fe_3O_4 nanoparticles, leading to aggregation inhibition due tothe steric hindrance and electrostatic repulsion. Therefore, citric acid is widely used as an anti-aggregation agent.

Magnetic fluids were originally developed by Papell of the United States National Aeronautics and Space Administration (NASA) in 1965 for position control of liquid fuel under zero gravity [11]. The initially developed magnetic fluid was prepared by ball-mill grinding of Fe_3O_4 grains in kerosene containing oleic acid for several hundred hours, followed by the removal of coarse particles by centrifugal separation. At present, various methods for synthesizing Fe_3O_4 nanoparticles using chemical reactions in gas, liquid, and solid phases have been developed. Among them, liquid phase synthesis has been actively studied because the component and concentration of the reactants can be controlled fairly easily and the formation reaction can progress, even under moderate conditions. In particular, coprecipitation methods that produce Fe_3O_4 by adding a base as a precipitant to a solution containing Fe^{2+} ions and Fe^{3+} ions are industrially employed because they can easily provide homogeneous Fe_3O_4 nanoparticles with smaller primary sizes [12]. The thermal decomposition method is also frequently used. Jeyadevan et al. [13] synthesized Fe_3O_4 nanoparticles that are suitable for magnetic hyperthermia via thermal decomposition of iron pentacarbonyl in oleic acid-containing dioctyl ether. Sun and Zeng [14] prepared mono-dispersed superparamagneticFe_3O_4 nanoparticles using iron acetylacetonate, oleic acid, and amine oleate. As a result, conventional methods can provide magnetic fluids that are desirable for various applications. For the previously

http://dx.doi.org/10.5772/66075

mentioned biomedical applications, water-based Fe_3O_4 magnetic fluids are suitable. However, in many cases, the conventional methods require iron salt, base, and organic solvents, requiring the removal of unnecessary components from the product to clean water-based magnetic fluids. This may increase the environmental impact and production cost. As a result, an innovative process is required to more readily prepare water-based Fe_3O_4 magnetic fluids without any additional operations.

To meet the demand, we developed a new mechanochemical process with an iron-free aqueous solution containing citric acid (CA) as a reaction accelerator and anti-aggregation agent milled at room temperature with a ball mill using steel balls, resulting in the production of water-based Fe_3O_4 magnetic fluid [15]. The formation of crystalline Fe_3O_4 nanoparticles in this process may consist of several steps, as follows: (1) corrosion of steel balls, (2) oxidation of released ferrous ions, (3) reduction of ferric ions, and (4) formation and crystal growth of Fe_3O_4. Therefore, the mechanochemical effect can enhance the formation and crystallization of Fe_3O_4. Furthermore, this method does not use iron salts as iron sources or a base as the precipitant because iron ions and hydroxide ions form during the corrosion, which can provide a water-based Fe_3O_4 magnetic fluid without any post-operations, such as the removal of unnecessary ions and solvent displacement.

This paper presents the properties of Fe_3O_4 magnetic fluids prepared by this mechanochemical process and a detailed analysis of the reaction mechanism based on changes in the composition of gas, liquid, and solid phases in the formation of Fe_3O_4 as well as ferrous, ferric, and hydroxide ions. Furthermore, the formation reaction of Fe_3O_4 is kinetically analysed under different gas phase conditions and mechanical energy fields.

2. Experimental

All chemicals used in this work were purchased from Wako Pure Chemical Industries and were used without further purification. Some preliminary experiments determined that the CA concentration in the starting solution was desirable to be 5 mmol/L, and a single Fe_3O_4 phase was finally obtained. Ninety millilitres of the CA solution (pH = 2.7) was placed in a tumbling ball mill consisting of a Teflon-lined gas-tight vessel (capacity 500 mL, diameter 90 mm) and carbon steel balls (Fe > 99 mass%, diameter 3 mm). The charged volume of the balls (includes the voids among balls) was 40% of the vessel capacity. The initial gas phase in the vessel was air at atmospheric pressure. The solution was milled at room temperature for anappropriate time period. The rotational speed of the vessel was 140 rpm, corresponding to the theoretically determined critical rotational speed. After milling, the fluid was removed from the vessel and characterized. The weight loss of balls during milling was also measured.

The particle size distribution and zeta potential of samples were determined using a particle size analyser (Malvern Zetasizer Nano ZS), and the phase evolution was evaluated using a powder X-ray diffractometer (Rigaku RINT-1500) after drying the sample. The average crystallite size was determined using Scherrer's equation for the diffraction peak from the Fe_3O_4 (311) plane at $2\theta = 35.4°$. The FT-IR spectrum was measured using a Fourier transform

infrared spectrophotometer (Shimadzu IRAffinity-1). The magnetic properties (i.e. magnetization-magnetic field hysteretic cycle) were analysed with a superconducting quantum interference device (SQUID) magnetometer (Quantum Design MPMS XL) at room temperature over a magnetic field range of −10 kOe to +10 kOe. The magnetic hyperthermia-related induction heating properties of the fluid were evaluated by an alternating magnetic field generator consisting of a radio frequency power source (Thamway T162-5723A), an impedance matching box (Thamway T020-5723F), and a solenoid coil (inner diameter 70 mm) with 21 copper tube (outer diameter of 4 mm and inner diameter of 3 mm) turns [13]. Cooling water flowed inside the copper tube. A proper amount (approximately 1.0 g) of fluid was charged in a glass tube with a diameter of 16 mm, and the test tube was placed in the coil centre. The temperature increase in the fluid from 37°C (corresponding to normal body temperature) in an alternating magnetic field was measured with an optical fibre thermometer (FISO Technologies FTI-10 equipped with FOT-L-NS-967). The frequency and amplitude of the magnetic field were 600 kHz and 3 kA/m, respectively.

In the analysis of the reaction mechanism, 0.5 mL of the gas in the vessel was sampled with a syringe after milling, and the gas component was analysed by a gas chromatograph (Shimadzu GC-8A). The pH of the resultant fluid was measured with a pH meter (Horiba D-21 equipped with 9625-10D electrode), and the iron(II) and iron(III) concentrations were determined by a colorimetric method with 1,10-phenanthroline and a spectrophotometer (JASCO Ubest V-530).

The influence of gas phase conditions in the vessel on the Fe_3O_4 formation was studied. The 5 mmol/L CA solution was placed in the vessel; then, compressed air was charged into the vessel before milling. The total pressure in the gas phase was varied from 1 atm (atmospheric pressure) to 6 atm, corresponding to initial oxygen partial pressures of 0.21–1.26 atm. The milling time was 24 h at total pressures lower than 2.5 atm but 48 h at higher than 3 atm. The pressure in the vessel before and after milling was measured, and the oxygen consumption was determined from the pressure change. Furthermore, the rotational speed of the vessel was varied from 0 to 140 rpm at a total pressure of 1 atm, which can alter the intensity of the mechanical energy field. Based on the obtained results, the kinetics of the Fe_3O_4 formation reaction were investigated.

Lastly, scaleup of the process was examined. In this investigation, a Teflon-lined milling vessel with a capacity of 2.6 L (diameter 150 mm) was used. The charged volume of the steel balls (diameter 3 mm) was 40% of the vessel capacity, and 476 mL of the 5 mmol/L CA solution was placed in the vessel and milled for 24 h. The gas phase was air at atmospheric pressure. The rotational speed of the large vessel was adjusted so that either the Froude number or the peripheral velocity in both vessels agreed with each other.

3. Results and discussion

3.1. Formation of Fe_3O_4 magnetic fluids

Figures 1 and **2** show the X-ray diffraction (XRD) patterns and average crystallite sizes of solid products obtained after milling the CA solution, respectively. At milling times of less

than 1.5 h, broad peaks that were attributed to ferrihydrite ($Fe_5O_8H{\cdot}4H_2O$), which is an amorphous or low crystalline oxyhydroxide [16–18], were observed in the XRD patterns. After 2 h, formation and crystal growth of Fe_3O_4 occurred, and milling for more than 18 h provided relatively high crystalline Fe_3O_4. However, most of the Fe_3O_4 particles settled in the fluid due to aggregation. To improve the dispersion, the total citrate concentration of fluids was increased by adding anhydrous CA and trisodium citrate dehydrate to the fluid obtained by milling for 18 h; and then the zeta potential was measured. The pH of the fluids was kept constant at approximately 8 in all fluids by adding proper amounts of CA and trisodium citrate. **Figure 3** illustrates the change in the zeta potential with the changing citrate concentration. The absolute value of the zeta potential increased with the increasing citrate concentration. When the citrate concentration was 14 mmol/L, corresponding to an iron/citrate molar ratio of approximately 3 in the fluid, the zeta potential was less than −40 mV, leading to good dispersion. It was inferred that an increase in the citrate concentration can improve the dispersion.

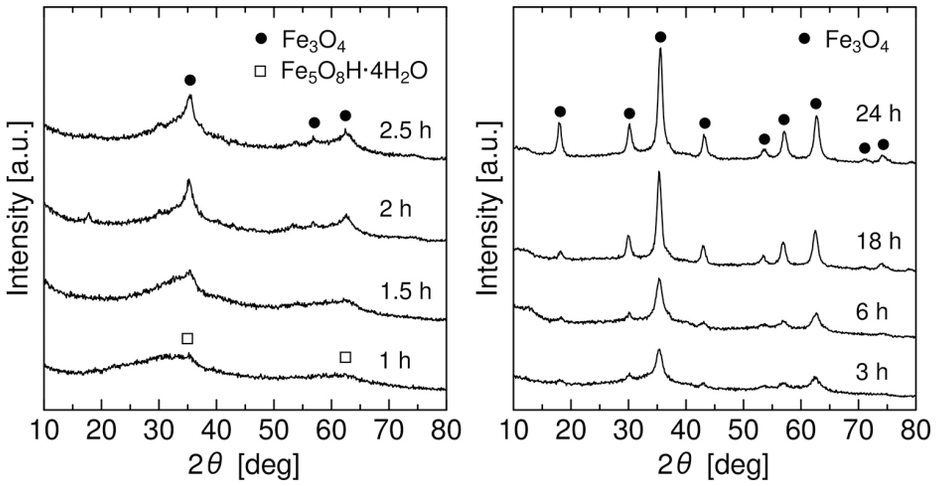

Figure 1. Effect of the milling time on the Fe_3O_4 phase evolution.

Using the fluid obtained at a milling time of 24 h, fluid with a total citrate concentration of 27 mmol/L was prepared and characterized. As shown in **Figure 4**, this fluid had good dispersion even after 2 weeks. Furthermore, when a permanent magnet was placed beside the glass bottle, the fluid was attracted to magnet, suggesting that the Fe_3O_4 nanoparticles have superparamagnetic properties. **Figure 5** shows the particle size distribution, magnetization-magnetic field curve, and FT-IR spectrum of the solid product obtained by drying the fluid after magnetic separation. The median diameter was 7.3 nm, while the crystallite size was 8.8 nm. The primary particle size was almost the same as the crystallite size, suggesting that the obtained Fe_3O_4 nanoparticles were monocrystalline. The saturation magnetization was 27 emu/g, which was much lower than that of bulk Fe_3O_4 (92 emu/g) due to the smaller particle size. The residual magnetization was approximately zero, and the coercivity was very low, indicating superparamagnetism. Additionally, some strong absorption bands in the FT-IR spectrum were observed, which were attributed to citrate ions, indicating that the Fe_3O_4

nanoparticle surface was modified by citrate ions. **Figure 6** illustrates a temperature adjustment of the fluid within 43 ± 0.5°C, corresponding to a typical temperature range in hyperthermia treatments, in an on-off-controlled alternating magnetic field. This fluid was found to exhibit good magnetic hyperthermia properties. In addition, the temperature was successfully controlled within the temperature range, suggesting that the fluid can be used in hyperthermia therapies.

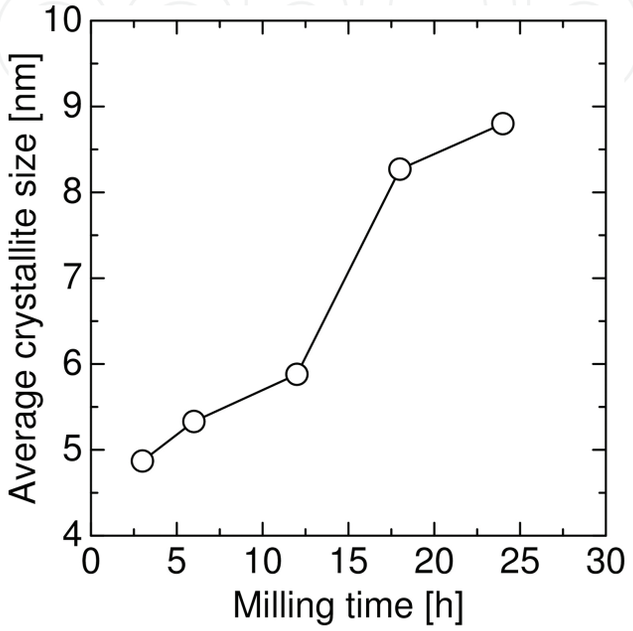

Figure 2. Change in the average crystallite size of Fe_3O_4 with milling time.

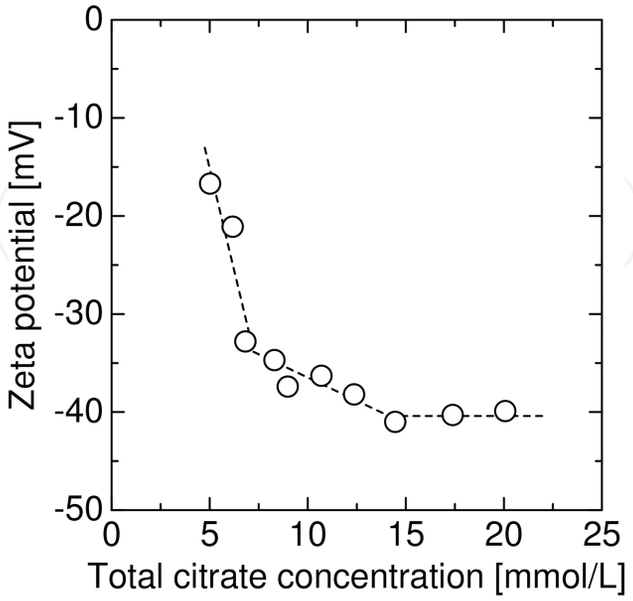

Figure 3. Effect of citrate concentration on the zeta potential of the fluid obtained with milling time of 18 h.

http://dx.doi.org/10.5772/66075

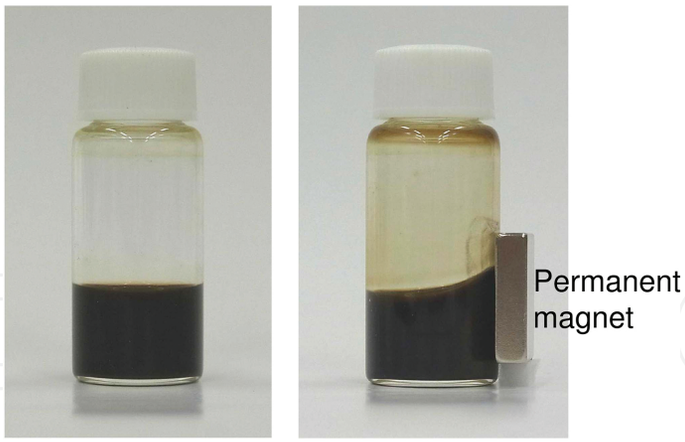

Figure 4. A fluid with a total citrate concentration of 27 mmol/L after 2 weeks.

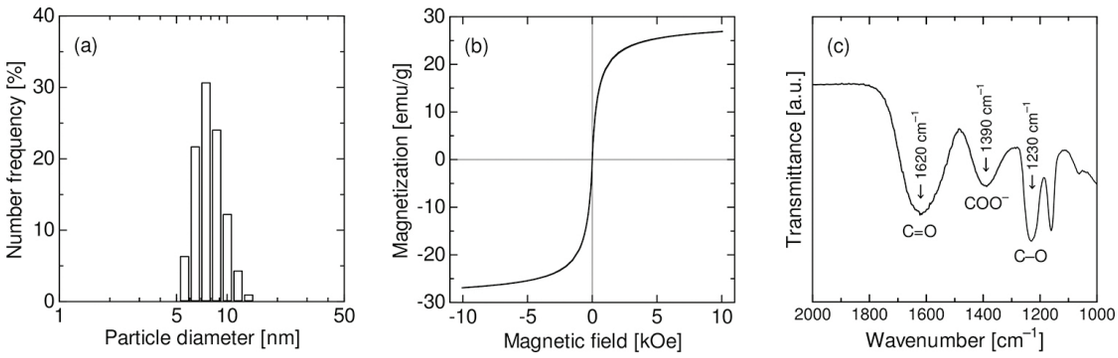

Figure 5. (a) Particle size distribution, (b) magnetization-magnetic field hysteresis cycle, and (c) FT-IR spectrum of the solid product.

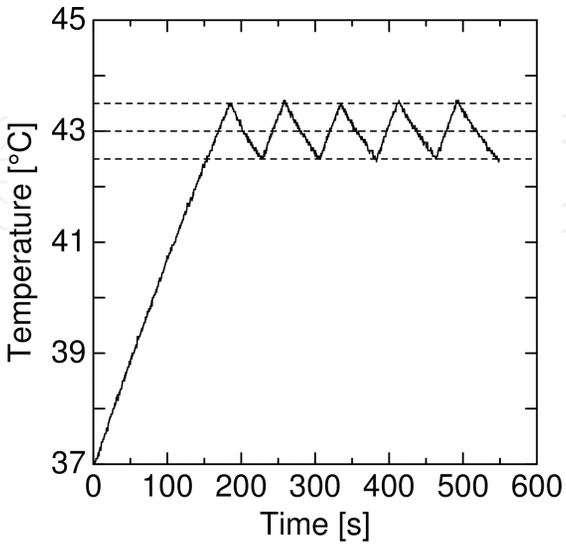

Figure 6. Temperature adjustment of the fluid in an on-off-controlled alternating magnetic field.

3.2. Reaction mechanism

Figure 7 shows the changes in the weight loss of balls and the iron concentration of the fluid with the milling time. With increasing milling time, the mass of the balls decreased and the iron concentrations increased, implying that ferrous (Fe^{2+}) ions were released from steel balls during milling due to corrosion, as expressed by Eq. (1).

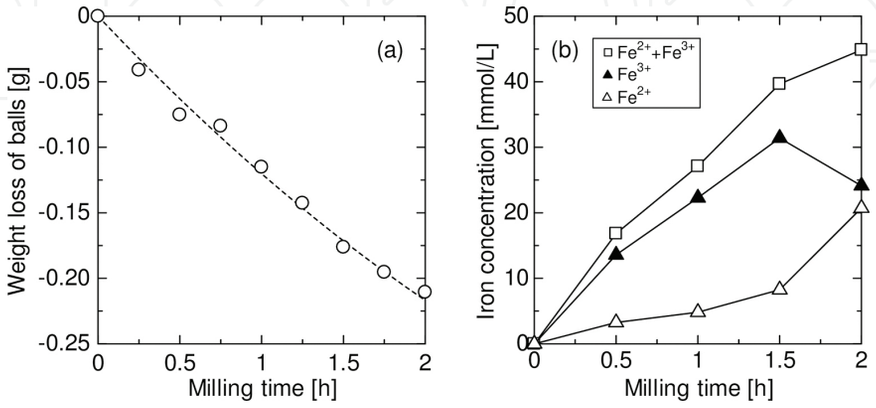

Figure 7. Change in the (a) weight loss of balls and (b) iron concentration with milling time at the initial stages.

$$Fe \rightarrow Fe^{2+} + 2e^{-} \tag{1}$$

Figure 8 shows the variation in the pH of fluids with the milling time. The fluid was acidic before milling and then immediately neutral. In general, free electrons (e^{-}) generated simultaneously with Fe^{2+} ion release are received by oxygen molecules (O_2) in a solution under acidic conditions, according to a cathode reaction expressed by Eq. (2).

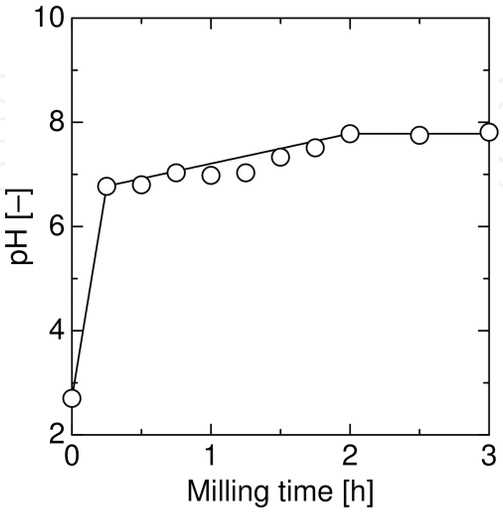

Figure 8. Change in the pH with milling time at the initial stages.

http://dx.doi.org/10.5772/66075

$$O_2 + 4H^+ + 4e^- \rightarrow 2H_2O \quad (2)$$

As hydrogen (H^+) ions in the solution are consumed, the solution pH increases and the solution becomes neutral. Under neutral conditions, the following cathode reaction occurs and hydroxide (OH^-) ions form.

$$O_2 + 2H_2O + 4e^- \rightarrow 4OH^- \quad (3)$$

On the other hand, released Fe^{2+} ions react with the OH^- ions formed according to Eq. (3), producing ferrous hydroxide ($Fe(OH)_2$) by Eq. (4).

$$Fe^{2+} + 2OH^- \rightarrow Fe(OH)_2 \quad (4)$$

As seen in **Figure 7**, most $Fe(OH)_2$ is immediately oxidized by dissolved O_2; then, ferric hydroxide ($Fe(OH)_3$) forms according to Eq. (5).

$$4Fe(OH)_2 + 2H_2O + O_2 \rightarrow 4Fe(OH)_3 \quad (5)$$

$Fe(OH)_3$ can be transformed to ferrihydrite ($Fe_5O_8H \cdot 4H_2O$) as below:

$$5Fe(OH)_3 \rightarrow Fe_5O_8H \cdot 4H_2O + 3H_2O \quad (6)$$

From Eqs. (1)–(6), Eq. (7) and Eq. (8) are obtained.

$$2Fe + O_2 + 2H_2O \rightarrow 2Fe(OH)_2 \quad (7)$$

$$20Fe(OH)_2 + 5O_2 \rightarrow 4Fe_5O_8H \cdot 4H_2O + 2H_2O \quad (8)$$

Eqs. (7) and (8) include O_2 as a reactant. Therefore, by analysing the dissolved O_2 concentration, the validity of the proposed reaction mechanism was confirmed. The dissolved O_2 concentration was estimated from the O_2 partial pressure in the gas phase using Henry's law:

$$p = Hx \quad (9)$$

where x is the molar fraction of O_2 in a liquid phase, p is the O_2 partial pressure in a gas phase in equilibrium with the liquid phase, and H is the Henry constant (= 4.38×10^4 atm at 25°C [19]).

In this process, the dissolved O_2 concentration can always vary during milling. However, the liquid phase is well mixed with the gas phase by milling, resulting in a relatively large gas-liquid interfacial area. Therefore, when the dissolved O_2 is consumed, O_2 can immediately be supplied from the gas phase. Accordingly, it can be assumed that the liquid and gas phases are always in equilibrium with each other. **Figure 9** shows the gas phase composition during milling. The open circles in this figure indicate the estimated values that were calculated using Eqs. (7) and (8) from the iron concentrations shown in **Figure 6**. It was confirmed that the volume of nitrogen (N_2) gas was almost constant and that hydrogen (H_2) gas evolution hardly occurred. In contrast, the O_2 gas was completely consumed within 2 h. Furthermore, the experimental data of the O_2 gas volume mostly agreed with the calculated values. The results demonstrate the validity of the reaction mechanism according to Eqs. (1)–(8).

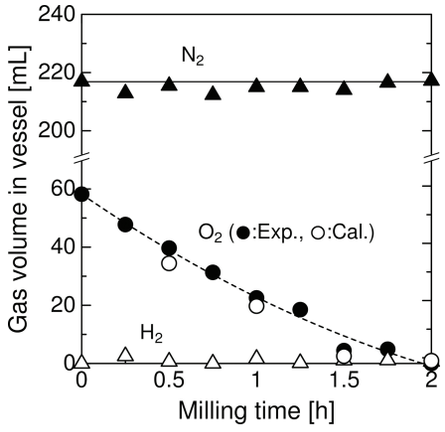

Figure 9. Change of the gas volumes in the vessel with milling time at the initial stages.

As seen in **Figure 8**, after 2 h, O_2 was absent from the vessel and the pH was almost constant at 7.8. **Figure 10** shows the change in the Fe^{2+} and Fe^{3+} ion concentrations with a milling time of up to 24 h. Fe^{3+} ions were reduced after 2 h. These results indicate that the free electrons formed at the steel corrosion are incorporated into $Fe_5O_8H \cdot 4H_2O$, namely Fe^{3+} ions are reduced, according to Eq. (10) instead of Eq. (3).

$$Fe_5O_8H \cdot 4H_2O + 3H_2O + 5e^- \rightarrow 5Fe(OH)_2 + 5OH^- \tag{10}$$

Although this chemical reaction produces OH^- ions, the OH^- ions can be completely consumed to form $Fe(OH)_2$ according to Eq. (4), which keeps the pH constant. In the absence of dissolved O_2, the formed $Fe(OH)_2$ can react with $Fe_5O_8H \cdot 4H_2O$ without being oxidized, resulting in the formation of Fe_3O_4 according to Eq. (11).

$$2Fe_5O_8H \cdot 4H_2O + 5Fe(OH)_2 \rightarrow 5Fe_3O_4 + 14H_2O \tag{11}$$

Consequently, the overall reaction under low O_2 conditions can be described by Eq. (12).

http://dx.doi.org/10.5772/66075

$$5Fe + 8Fe_5O_8H \cdot 4H_2O \rightarrow 15Fe_3O_4 + 36H_2O \quad (12)$$

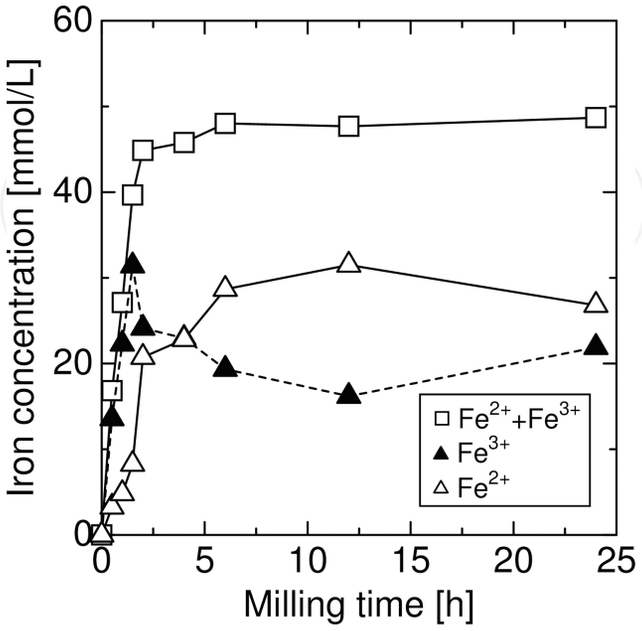

Figure 10. Change in iron concentrations with a milling time of up to 24 h.

Figure 11 illustrates the evolution of H_2 during milling. The formation of H_2 was noticed for long milling times. As seen in **Figure 10**, the iron concentrations slightly increased even after 6 h. Thus, the following reduction reaction may occur, resulting in H_2 evolution.

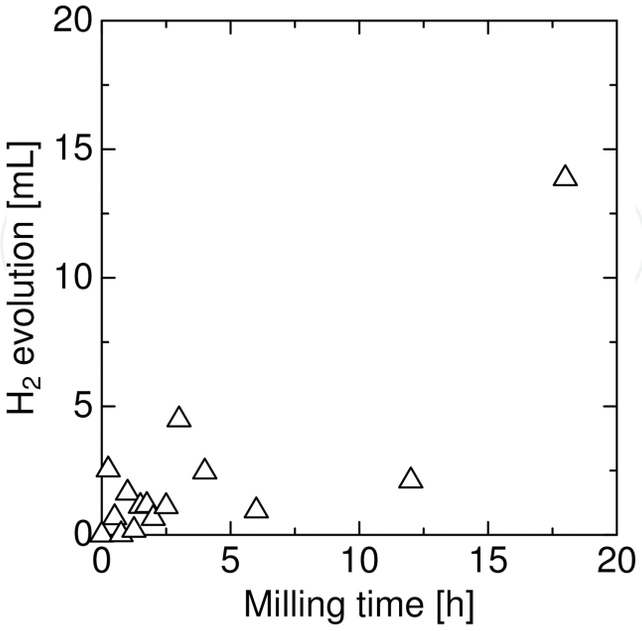

Figure 11. Evolution of H_2 during milling.

$$2H_2O + 2e^- \rightarrow 2OH^- + H_2 \tag{13}$$

OH^- ions thus formed react with Fe^{2+} ions, resulting in the formation of $Fe(OH)_2$. According to Eq. (4), $Fe(OH)_2$ can transform to Fe_3O_4 according to Eq. (14).

$$3Fe(OH)_2 \rightarrow Fe_3O_4 + 2H_2O + H_2 \tag{14}$$

From Eqs. (1), (4), (13), and (14), Eq. (15) is derived as the overall reaction for the formation of Fe_3O_4:

$$3Fe + 4H_2O \rightarrow Fe_3O_4 + 4H_2 \tag{15}$$

In summary, it has been established that a magnetic fluid consisting of well-dispersed superparamagnetic Fe_3O_4 nanoparticles can be formed by milling a CA solution with steel balls, according to the following reaction mechanism.

1. Under high O_2 conditions, milling the solution can result in an immediate mass transfer of O_2 from the gas phase to the liquid phase. Fe^{2+} ions are released from the steel balls. At the same time, using formed free electrons, OH^- ions are produced from O_2 and H_2O and then react with Fe^{2+} ions, resulting in the formation of $Fe(OH)_2$. $Fe(OH)_2$ is oxidized by dissolved O_2; then, $Fe_5O_8H \cdot 4H_2O$ forms.

2. Under low O_2 conditions, $Fe_5O_8H \cdot 4H_2O$ is reduced to $Fe(OH)_2$, and the reaction between $Fe(OH)_2$ and $Fe_5O_8H \cdot 4H_2O$ produces Fe_3O_4.

3. After the consumption of $Fe_5O_8H \cdot 4H_2O$, OH^- ions and H_2 are produced via reduction of H_2O. $Fe(OH)_2$ forms from Fe^{2+} and OH^- ions, and Fe_3O_4 and H_2 are produced from $Fe(OH)_2$.

3.3. Effect of the oxygen partial pressure

Figures 12–14 illustrate the XRD pattern of the obtained solid products, pH after milling, and internal pressure change of the vessel, respectively, under various initial total pressures in the vessel. Regardless of the internal total pressure, crystalline Fe_3O_4 was obtained, and the pH after milling was approximately 9. As seen in **Figure 14**, the internal pressure change was in agreement with the theoretical values (shown by a broken line) that had been calculated by assuming that O_2 in the vessel was completely consumed during milling, suggesting that under an initial oxygen partial pressure of less than 1.26 atm, O_2 was used in the Fe_3O_4 formation process.

From Eqs. (1), (3)–(6), and (11), the overall reaction for Fe_3O_4 formation under neutral and high O_2 conditions is expressed by Eq. (16).

http://dx.doi.org/10.5772/66075

$$3Fe + 2O_2 \rightarrow Fe_3O_4 \tag{16}$$

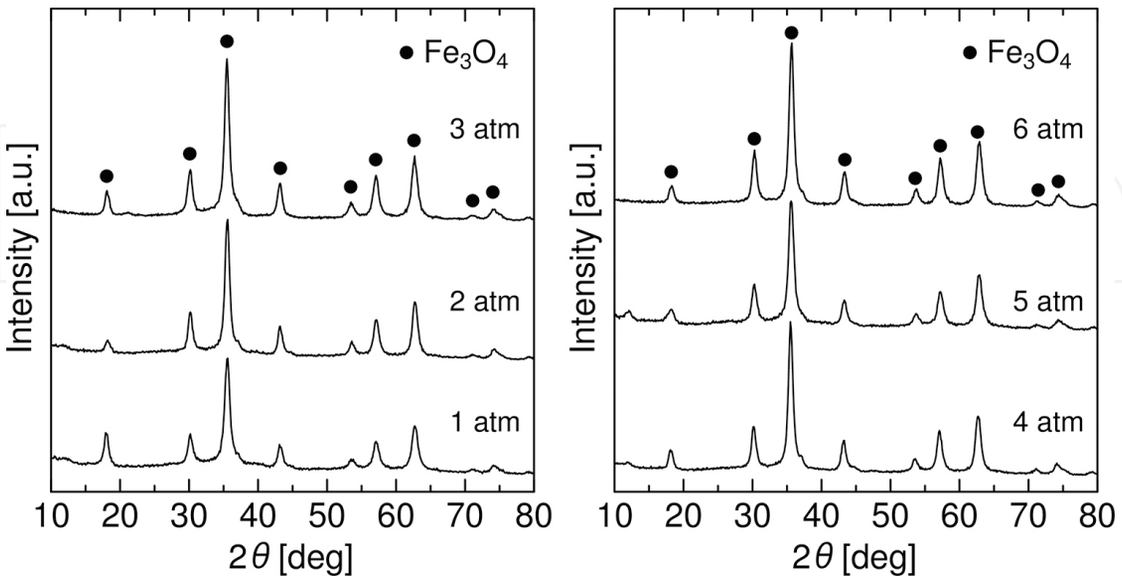

Figure 12. Effect of the initial total pressure on Fe_3O_4 phase evolution.

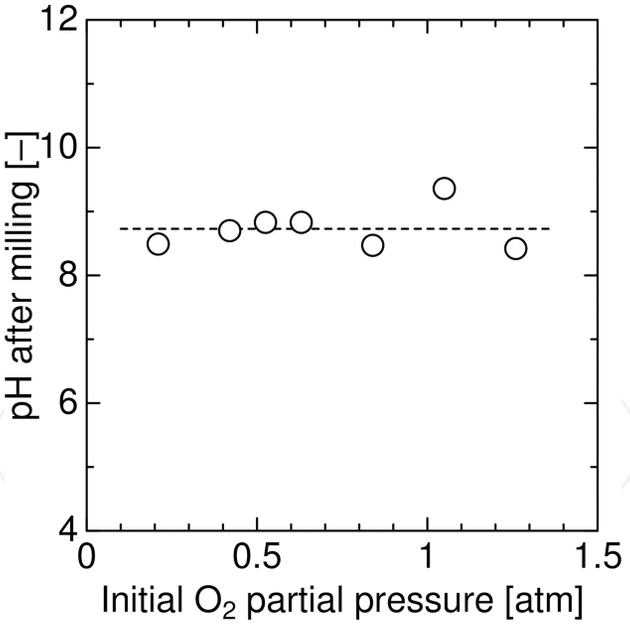

Figure 13. Change in the pH after milling with the initial O_2 partial pressure.

Figure 15 shows the iron concentration of fluids estimated based on the internal pressure change, as shown in **Figure 14** with Eq. (16). The iron concentration increased with increasing initial O_2 partial pressure, indicating that the iron concentration can be controlled by the initial O_2 partial pressure.

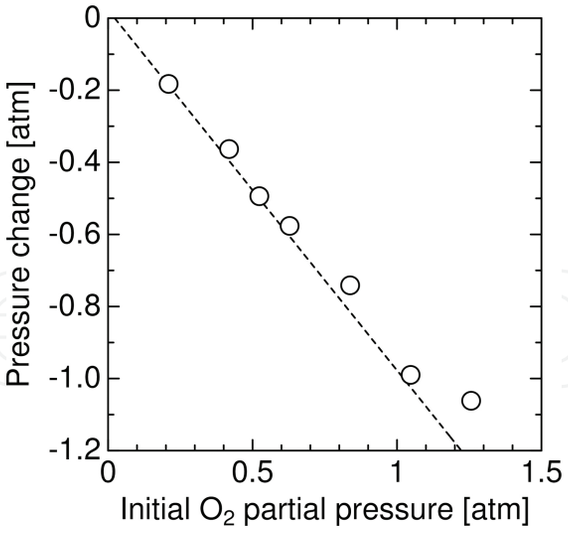

Figure 14. Change in the pressure after milling with the initial O_2 partial pressure.

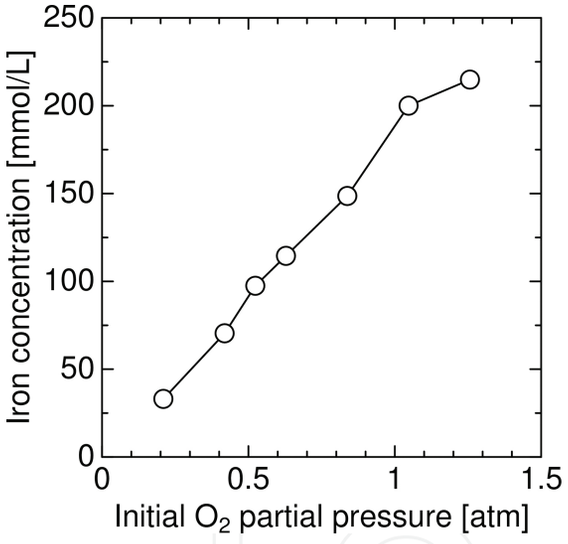

Figure 15. Change in the estimated iron concentration with the initial O_2 partial pressure.

3.4. Kinetics of the reaction for the formation of Fe_3O_4

Based on the concentrations of Fe^{2+} and Fe^{3+} ions during milling, the Fe_3O_4 formation reaction was kinetically analysed. **Figure 16** shows the change in the O_2 partial pressure and iron concentrations with the milling time in the initial stages at an initial total pressure of 1 atm. A monotonous decrease in the O_2 partial pressure with increased milling time was observed. Because the dissolved O_2 concentration is proportional to the O_2 partial pressure, the rate of reactions related to the dissolved O_2 concentration, as shown by Eqs. (7) and (8), can also vary depending on the milling time. However, at less than 1.5 h, O_2 was consumed at a constant rate, and the rates of Fe^{2+} and Fe^{3+} ion formation were almost constant regardless of the milling

http://dx.doi.org/10.5772/66075

time, as seen in **Figure 7**b. The results imply that the reactions are independent of the dissolved O_2 concentration. Therefore, the reaction rates of Eqs. (7) and (8) can be described by a zero-order model. This model is effective because O_2 quickly dissolves into the solution due to vigorous gas-liquid mixing by milling and milling accelerates the corrosion of steel due to the improvement in the diffusion rate of O_2 to the steel surface. Accordingly, the Fe_3O_4 formation process may be the oxidation-reduction reaction control, and both the dissolution of O_2 from the gas phase to the liquid phase and diffusion rate of O_2 in the liquid phase can be much faster than the rate of the oxidation-reduction reaction.

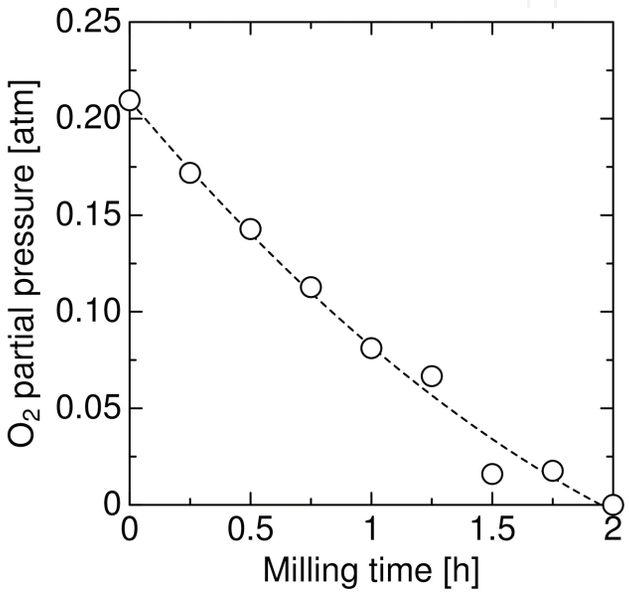

Figure 16. Changes in the O_2 partial pressure with milling time at an initial total pressure of 1 atm.

Using the data shown in **Figure 16**, the rates of Fe^{2+} and Fe^{3+} ion formation were calculated. Based on Eqs. (7) and (8), the O_2 consumption rate was determined to be approximately 0.40 μmol/s, which nearly agreed with the experimental data (0.41 μmol/s) shown in **Figure 16**. This result suggests that the consumed O_2 was spent on the release and oxidation of Fe^{2+} ions.

Eqs. (7) and (8) are rewritten as follows:

$$Fe + \frac{1}{2}O_2 + H_2O \rightarrow Fe(OH)_2 \tag{17}$$

$$Fe(OH)_2 + \frac{1}{4}O_2 \rightarrow \frac{1}{5}Fe_5O_8H \cdot 4H_2O + \frac{1}{10}H_2O \tag{18}$$

Assuming that the reaction rates of Eqs. (17) and (18), r_1 and r_2, can be described by a zero-order model and expressed as follows:

$$r_1 = k_1 \tag{19}$$

$$r_2 = k_2 \tag{20}$$

Here k_1 and k_2 are the rate constants of Eqs. (17) and (18), respectively. As a result, the rate of $Fe(OH)_2$ formation reaction, r, can be expressed by Eq. (21).

$$r = r_1 - r_2 = k_1 - k_2 = K \tag{21}$$

K indicates the rate constant of the overall $Fe(OH)_2$ formation reaction.

Figure 17 shows the change in the O_2 partial pressure with a milling time of up to 24 h. Regardless of the milling time, the rate of O_2 consumption was constant under all of the initial total pressures. **Figure 18** illustrates the rate constant K calculated using Eqs. (19)–(21) as a function of the initial O_2 partial pressure. K was found to decrease with the increasing initial O_2 partial pressure. As shown in **Figure 19**, when the initial O_2 partial pressure was relatively high, goethite (α-FeOOH) and $Fe_5O_8H \cdot 4H_2O$ formed as intermediates. In general, the rate of steel corrosion is affected by the mass fraction of iron oxyhydroxides and iron oxides in a corrosion product on the steel. In particular, when a high level of α-FeOOH is contained in the corrosion product, the corrosion rate can decrease because α-FeOOH prevents O_2 from penetrating into the steel surface [20]. At high initial O_2 partial pressures, $Fe_5O_8H \cdot 4H_2O$ can make a phase transition to α-FeOOH, and a dense corrosion product layer may form on the steel surface. This inhibits the mass transfer of O_2, resulting in a decrease in the rate of $Fe(OH)_2$ formation reaction.

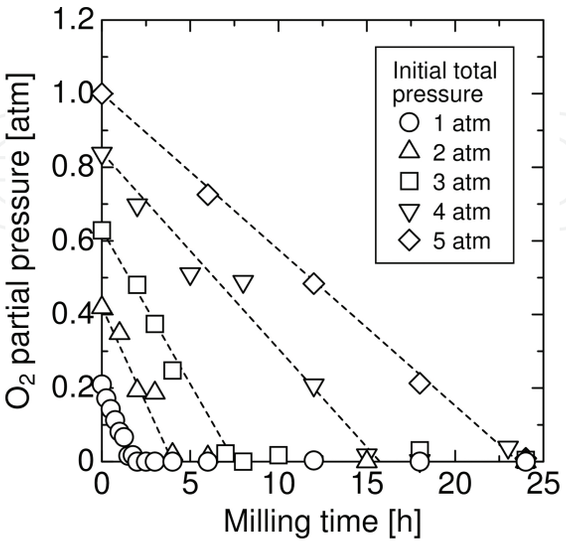

Figure 17. Change in the O_2 partial pressure with a milling time of up to 24 h.

http://dx.doi.org/10.5772/66075

Next, the effect of the vessel rotational speed on the O_2 consumption was studied in atmospheric pressure. **Figure 20** depicts the change in the O_2 partial pressure with the milling time. The O_2 consumption rate was almost the same, regardless of the rotational speed. **Figure 21** illustrates the relationship between the rotational speed and *K* calculated assuming that the O_2 consumption can be expressed by a zero-order equation. At rotational speeds higher than 10 rpm, *K* was almost constant, suggesting that the milling generated a sufficient level of energy required for the mass transfer and consumption of O_2, even at low rotational speeds.

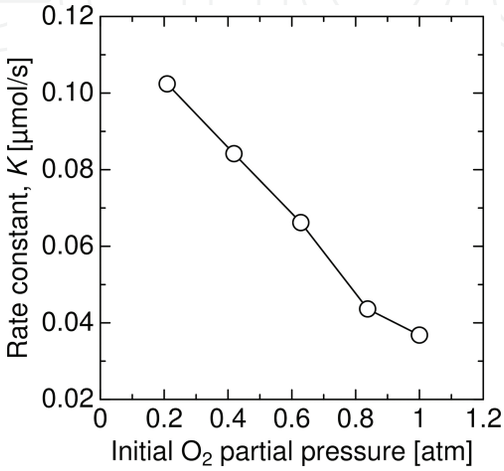

Figure 18. Change in the rate constant *K* with an initial O_2 partial pressure.

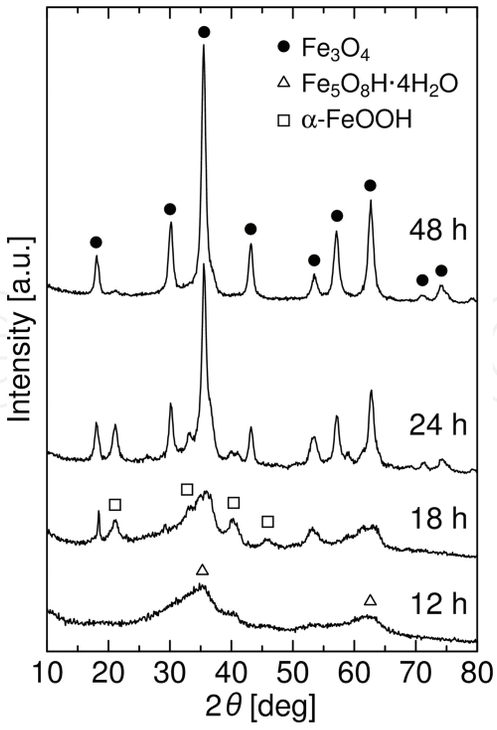

Figure 19. XRD patterns of a solid product obtained at an initial total pressure of 3 atm.

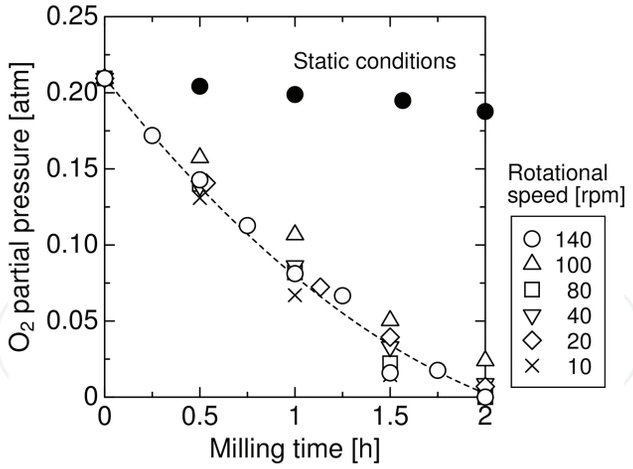

Figure 20. Effect of the rotational speed on the O_2 partial pressure after milling.

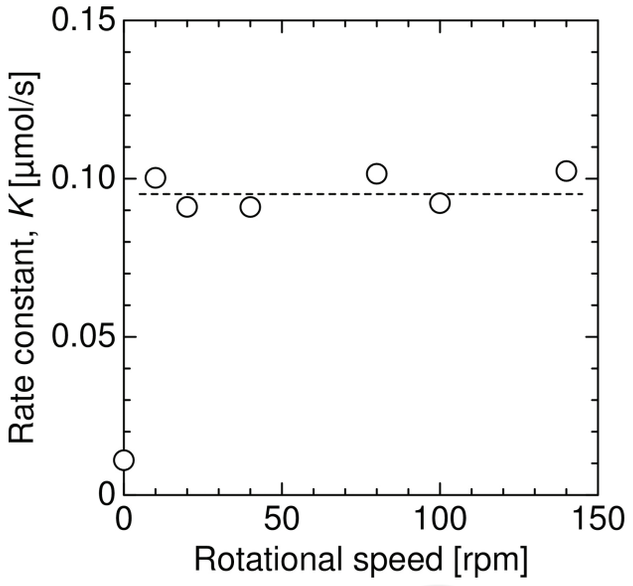

Figure 21. Effect of the vessel rotational speed on the rate constant *K*.

3.5. Scaleup of the process

Using a milling vessel with a capacity of 2.6 L, which was approximately 5 times as large as the small vessel used in the above investigations, the scaleup of the process was studied based on two cases, constant Froude number and constant peripheral velocity of the vessels. The rotational speed of 140 rpm for the small vessel corresponds to 108.4 rpm for the large vessel at a constant Froude number (= 0.0500) and 87.7 rpm at a constant peripheral velocity (= 0.735 m/s). **Figures 22–24** show the XRD pattern of solid products, average crystallite size, and pH after milling, respectively. The results demonstrate that the large scale process can fabricate a similar fluid, suggesting that scale-up of the process can be successful based on either the Froude number or peripheral velocity of the vessel.

http://dx.doi.org/10.5772/66075

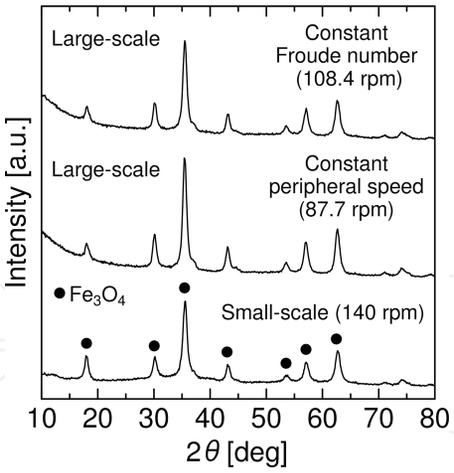

Figure 22. XRD patterns of solid products obtained in both processes.

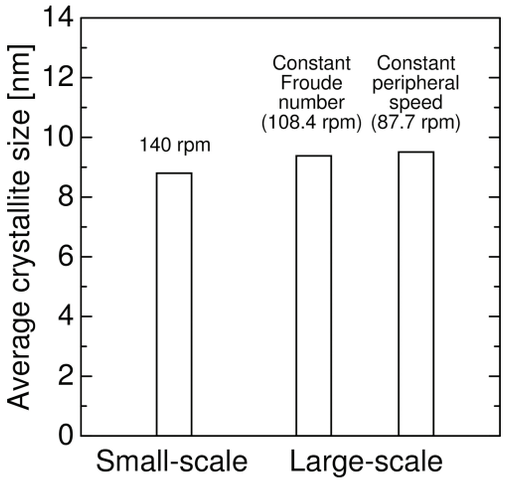

Figure 23. Comparison of the average crystallite size of solid products obtained in both processes.

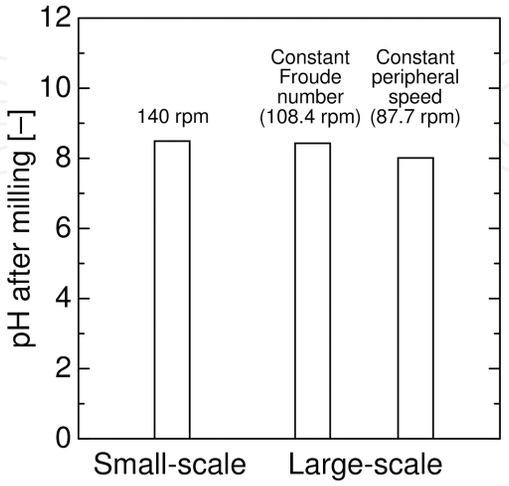

Figure 24. Comparison of the final pH of fluids obtained in both processes.

4. Conclusions

This study analysed in detail a new mechanochemical process for readily synthesizing water-based magnetic Fe_3O_4 fluids. Major conclusions are summarized as follows:

a. The Fe_3O_4 formation mechanism in this process has been clarified, which can be described by several oxidation-reduction reactions, such as the corrosion of steel, oxidation of $Fe(OH)_2$, and reduction of $Fe_5O_8H \cdot 4H_2O$. Additionally, O_2 plays an important role in the reaction mechanism.

b. The Fe_3O_4 concentration of fluids can be controlled by the initial O_2 partial pressure in the vessel.

c. Kinetic analysis of the process clarified the effects of the dissolved O_2 and the vessel rotational speed on the rate of the $Fe(OH)_2$ formation reaction. In the process, the reaction rate of O_2 consumption can be expressed by a zero-order equation.

d. Scaleup of the process can be successful by considering either the Froude number or peripheral velocity of the vessel.

Acknowledgements

This work was financially supported by JSPS KAKENHI Grant Number JP24686090. The author thanks Mr. Tsukasa Kagawa for his supports during the experiments.

Author details

Tomohiro Iwasaki

Address all correspondence to: iwasaki@chemeng.osakafu-u.ac.jp

Osaka Prefecture University, Sakai, Japan

References

[1] Mitamura Y. Medical applications of magnetic fluids. J Jpn Soc Prec Eng. 2006;72:834–837.

[2] Tiefenauer LX, Tschirky A, Kühne G, Andres RY. In vivo evaluation of magnetite nanoparticles for use as a tumor contrast agent in MRI. Magn Reson Imaging. 1996;14:391–402.

[3] Lima-Tenório MK, Gómez Pineda EA, Ahmad NM, Fessi H, Elaissari E. Magnetic nanoparticles: In vivo cancer diagnosis and therapy. Int J Pharm. 205;493:313–327.

[4] Mürbe J, Rechtenbach A, Töpfer J. Synthesis and physical characterization of magnetite nanoparticles for biomedical applications. Mater Chem Phys. 2008;110:426–433.

[5] Moghimi SM, Hunter AC, Murray JC. Long-circulating and target-specific nanoparticles: Theory to practice. Pharmacol Rev. 2001;53:283–318.

[6] Matsumura Y, Maeda H. A new concept for macromolecular therapeutics in cancer chemotherapy: Mechanism of tumoritropic accumulation of proteins and the antitumor agent smancs. Cancer Res. 1986;46:6387–6392.

[7] Wen X, Yang J, He B, Gu Z. Preparation of monodisperse magnetite nanoparticles under mild conditions. Curr Appl Phys. 2008;8:535–541.

[8] Zhang F, Su Z, Wen F, Li F. Synthesis and characterization of polystyrene-grafted magnetite nanoparticles. Colloid Polym Sci. 2008;286:837–841.

[9] Frimpong RA, Dou J, Pechan M, Hilt JZ. Enhancing remote controlled heating characteristics in hydrophilic magnetite nanoparticles via facile co-precipitation. J Magn Magn Mater. 2010;322:326–331.

[10] Elisa de Sousa M, Fernández van Raap MB, Rivas PC, Mendoza Zélis P, Girardin P, Pasquevich GA, Alessandrini JL, Muraca D, Sánchez FH. Stability and relaxation mechanisms of citric acid coated magnetite nanoparticles for magnetic hyperthermia. J Phys Chem C. 2013;117:5436–5445.

[11] Papell SS. Low viscosity magnetic fluid obtained by the colloidal suspension of magnetic particles. U.S. Patent 3215572. 1965.

[12] Kim DK, Zhang Y, Voit W, Rao KV, Muhammed M. Synthesis and characterization of surfactant-coated superparamagnetic monodispersed iron oxide nanoparticles. J Magn Magn Mater. 2001;225:30–36.

[13] Jeyadevan B. Present status and prospects of magnetite nanoparticles-based hyperthermia. J Ceram Soc Jpn. 2010;118:391–401.

[14] Sun S, Zeng H. Size-controlled synthesis of magnetite nanoparticles. J Am Chem Soc. 2002;124:8204–8205.

[15] Iwasaki T, Kagawa T, Nakamura H, Watano S. Control of aggregation and dispersion of mechanochemically synthesized magnetite nanoparticles in aqueous magnetic fluid. In: Proceedings of the 10th International Symposium on Agglomeration (Agglos 10); 2–4 September 2013; Kobe.

[16] Zhao J, Huggins FE, Feng Z, Lu FL, Shah N, Huffman GP. Structure of a nanophase iron oxide catalyst. J Catal. 1993;143:499–509.

[17] Feng Z, Zhao J, Huggins FE, Huffman GP. Agglomeration and phase transition of a nanophase iron oxide catalyst. J Catal. 1993;143:510–519.

[18] Zhao J, Huggins FE, Feng Z, Huffman GP. Ferrihydrite; surface structure and its effects on phase transformation. Clay Clay Miner. 1994;42:737–746.

[19] Han KN. Fundamentals of Aqueous Metallurgy. Littleton: Society for Mining, Metallurgy, and Exploration; 2002. 197 p.

[20] Yamashita M, Maeda A, Uchida H, Kamimura T, Miyuki H. Crystalline rust compositions and weathering properties of steels exposed in nation-wide atmospheres for 17 years. J Jpn Inst Metals. 2001;65:967–971.